npj computational materials

www.nature.com/npjcompumats

ARTICLE OPEN

Check for updates

Giant multiphononic effects in a perovskite oxide

Claudio Cazorla[1], Massimiliano Stengel[2,3], Jorge Íñiguez[4,5] and Riccardo Rurali[2]✉

Perovskite oxides offer tremendous potential for applications in information storage and energy conversion, owing to a subtle interplay between their spin, charge, orbital and lattice degrees of freedom. Here, we further expand the possible range of perovskite oxides operation towards the fields of thermal management and thermal computing by exploiting an exceptional synergy between different ferroic orders. We propose dynamical control of the heat flow in a distinctive family of perovskite oxides obtained via the application of small electric (~10 kV/cm) and/or magnetic (~1 T) fields. Based on first-principles simulations, we predict a relative heat conductivity variation of ~100% in $SrMnO_3$ thin films near room temperature resulting from a phase transition that involves huge changes in both the magnetization and electric polarization. The disclosed giant multiphononic effects are fundamentally caused by anharmonic spin-phonon couplings that strongly influence the mean lifetime of phonons.

npj Computational Materials (2023)9:97 ; https://doi.org/10.1038/s41524-023-01057-w

INTRODUCTION

Phonons govern thermal transport in insulators and semiconductors; hence, the ability to control their propagation is key to a number of applications ranging from thermal management[1] to thermoelectrics[2,3], besides conveying great fundamental interest. Manipulating phonons via external fields is attracting increasingly more attention, since it may enable fast and reliable dynamical tuning of the thermal conductivity in materials, thus bringing on the design of phononic devices, such as thermal diodes[4] and thermal transistors[5], and the development of phonon-based information technologies[6,7].

Electric[8–14] and magnetic[15] fields can be used to act upon the crystal lattice of polar and magnetic materials, respectively, and thus impact their thermal conductivity by either modifying the corresponding phonon dispersion relations (i.e., phonon energies and velocities) and/or phonon lifetimes (i.e., anharmonic phonon-phonon interactions). In this context, the most desirable situation occurs when an external field drives a structural phase transition, since very large changes in the thermal conductivity can then be expected. However, field-driven phase transitions are not always possible or practical. Indeed, even when transitions between different polar and magnetic states are conceivable, the involved energy barriers may be so high that the necessary triggering fields turn out to be unfeasible from a practical point of view.

In this article, we predict the realization of extreme phononic variations induced by small electric (~10 kV/cm) and magnetic (~1 T) fields in a perovskite oxide. We dub these effects as *multiphononic* in analogy to multiferroics[16] and multicaloric[17], meaning that the vibrational properties of a material, such as phonon frequencies, phonon velocities and/or phonon lifetimes, can be noticeably altered by two or more different types of external fields. Specifically, we study $SrMnO_3$ (SMO), a compound that in bulk presents a non-polar structure and G-type antiferromagnetism (AFM) below $T_N \approx 233-260$ K[18–20]; by contrast, under appropriate epitaxial strain conditions, SMO displays coexisting and coupled ferromagnetic and ferroelectric features[21]. The multiphononic effects disclosed here for SMO thin films on the verge of a magnetoelectric phase transition are giant, as shown by a heat conductivity change of 75–200% (depending on the temperature). We explain the underlying causes of such physical effects in terms of phonon scattering processes and spin-phonon couplings.

Analogous multiphononic effects to those reported here for SMO can be expected to occur also in other akin perovskite oxide thin films in which epitaxial strain may similarly drive magnetoelectric phase transitions (e.g., $BiFeO_3$ and $BiCoO_3$)[22–24]. Thus, our work proposes a strategy for significantly manipulating phonons and thermal transport in perovskite oxides that is based on the combination of epitaxial strain and moderate external fields.

RESULTS AND DISCUSSION

SMO phase diagram: bulk and thin films

Bulk SMO is assumed to crystallize in a cubic $Pm\bar{3}m$ structure[25] that is centrosymmetric and therefore does not exhibit any electric polarization. Nevertheless, it was first theoretically predicted by means of first-principles calculations, and later demonstrated in experimental temperature-dependent ferroelectric and magnetic studies, that under tensile epitaxial strain SMO presents a multiferroic phase in which both ferroelectricity and antiferromagnetic spin ordering coexist and are strongly coupled[21,26]. On the theoretical side, Lee and Rabe reported the stabilization of a ferroelectric orthorhombic phase with *Ima2* symmetry under small epitaxial strains of $\eta \equiv a_{in}/a_{in,0} - 1 \approx +1\%$ (where $a_{in,0}$ stands for the equilibrium lattice parameter of bulk SMO) exerted on the (001) plane[21]. This orthorhombic structure displays an electric polarization (P) oriented along the pseudo-cubic [110] direction, antiphase antiferrodistortive oxygen octahedral rotations (AFD O_6) about the [110] axis, and G-type AFM order. (Throughout we assume a pseudocubic setting.) Thus, in terms of its various order parameters this phase can be labeled as Γ[110]+R[110]-G, where Γ refers to the electric polarization and R to the AFD O_6 tilts (see Fig. 1a). In Glazer's notation, the R[110] (R[001]) distortion is denoted by $a^-a^-c^0$ ($a^0a^0c^-$).

Interestingly, a series of magnetic transitions driven by an increasing tensile strain, η, eventually leading to ferromagnetic

[1]Departament de Física, Universitat Politècnica de Catalunya, Campus Nord B4-B5, Barcelona 08034, Spain. [2]Institut de Ciència de Materials de Barcelona, ICMAB–CSIC, Campus UAB, 08193 Bellaterra, Spain. [3]ICREA-Institució Catalana de Recerca i Estudis Avançats, 08010 Barcelona, Spain. [4]Materials Research and Technology Department, Luxembourg Institute of Science and Technology (LIST), Avenue des Hauts-Fourneaux 5, L-4362 Esch/Alzette, Luxembourg. [5]Department of Physics and Materials Science, University of Luxembourg, 41 Rue du Brill, L-4422 Belvaux, Luxembourg. ✉email: rrurali@icmab.es

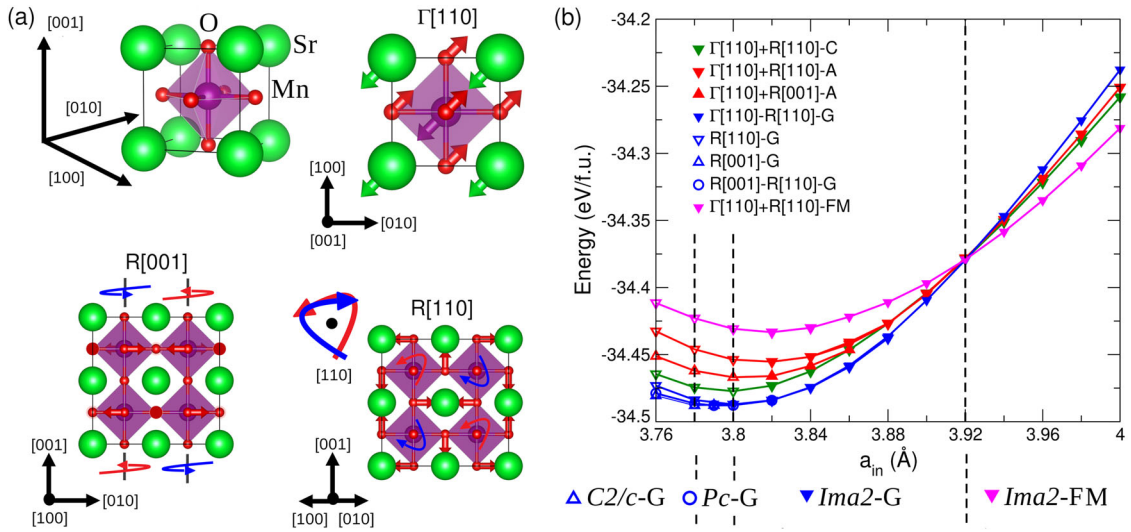

Fig. 1 Phase transitions in $SrMnO_3$ thin films induced by [110] epitaxial strain. a Sketch of the usual 5-atom perovskite oxide unit cell displaying cubic symmetry (i.e., non-polar). Sr, Mn and O atoms are represented with green, purple and red spheres, respectively. Polar Γ[110] and non-polar antiferrodistortive R[001] and R[110] distortions involving all-ion displacements and oxygen octahedral anti-phase rotations, respectively, are represented with straight and curly arrows. **b** DFT energy calculations for several competitive SMO phases expressed as a function of in-plane lattice parameter. Symbols indicate different type of AFD O_6, colors indicate different magnetic ordering, and filled (empty) symbols indicate polar (non polar) phases. For those phases that are polar for $a_{in} \geq 3.82$, but non polar for $a_{in} < 3.82$ (e.g. $\Gamma[110] + R[110] - C$), we omit the label of the latter for simplicity). a_{in} values at which a η-induced phase transition occurs are indicated with dashed vertical lines. The space group of the crystal phases stabilized by effect of epitaxial strain are indicated along with the corresponding magnetic spin ordering (G, C, A and FM).

spin ordering (FM), were also reported for this material, namely, G-type AFM → C-type AFM → A-type AFM → FM[21]. Therefore, SMO thin films are one of the few known multiferroic systems in which ferroelectricity and strong ferromagnetism are expected to coexist. On the experimental side, large epitaxial strains of +3.8% have been realized in SMO thin films with the reassuring findings of high-temperature ferroelectricity and strong spin-phonon couplings[26].

We have theoretically revisited the phase diagram of SMO in bulk and thin-film geometries by using first-principles computational methods analogous (although not identical) to those employed by Lee and Rabe[21] (see "Methods"). Besides the usual tetragonal and orthorhombic phases, in our analysis we have also considered monoclinic structures; in addition, we have explored an ample range of compressive epitaxial strains (i.e., $\eta \leq 0$). In general, the results of our first-principles calculations are consistent with those of previous works since they reproduce the stabilization of a ferroelectric *Ima2* phase with FM spin ordering at large and positive η's (Fig. 1). In our case, however, the isomorphic C-type and A-type AFM phases, although competitive, never become the ground state (Fig. 1b); hence the only phase transition that we observe under tensile strain is *Ima2*-G → *Ima2*-FM, occurring at $a_{in} = 3.92$ Å.

Remarkably, this magnetic phase transition is accompanied by a two-fold increase in the electric polarization, which grows from 22.6 μC/cm^2 in the AFM phase to 43.5 μC/cm^2 in the FM phase (see Supplementary Fig. 1). A simultaneous and significant increment of the AFD O_6 tilts (i.e., R[110] distortion) also occurs: the characteristic rotation angle is about two times larger in the FM phase than in the AFM (Fig. S2). Thus, an unusual cooperative Γ–R distortion interplay mediated by spin ordering is found in the *Ima2* phase that tends to favor the in-plane polarization. Besides its multifunctional interest emphasized below, this finding is consistent with the experimental observation of strong spin-lattice couplings[26]. Thus, in the vicinity of $a_{in} = 3.92$ Å, SMO thin films are on the verge of a magnetoelectric phase transition in which both the magnetic and ferroelectric order parameters (as well as the AFD one) may change very abruptly. Closer inspection of the phase diagram reveals that around $a_{in} = 3.92$ Å the energies of the four *Ima2* phases exhibiting distinct magnetic orderings are practically identical; this finding indicates that the interactions between magnetic spins are effectively vanishing and therefore their orientation might be easily adjusted by an external magnetic field. Meanwhile, the structural traits of the four magnetic *Ima2* phases are plainly different in terms of the polar and AFD distortions.

As for compressive epitaxial strains, our first-principles calculations reveal the stabilization of two monoclinic phases that, to the best of our knowledge, have not been reported before for SMO (Figs. 1, S3). At small in-plane lattice parameters $a_{in} \leq 3.78$ Å, we find the ground state of the system to be a non-polar monoclinic phase exhibiting *C2/c* symmetry, with prominent antiphase AFD O_6 rotations about the out-of-plane direction (Fig. S4) and G-type AFM order (labeled as R[001]-G in Fig. 1b). Intriguingly, these AFD distortions get reinforced under increasing compressive strain and no traces of polar instabilities are found for this phase down to an in-plane lattice parameter of 3.70 Å (not shown here). Nonetheless, it may not be discarded that other polar phases, different from those considered in this study, could be stabilized under medium and large compressive strain conditions (although the feasibility to check this possibility in practice is quite reduced due to the scarcity of substrates presenting such small in-plane lattice parameters[27]). In the narrow interval $3.78 \leq a_{in} \leq 3.80$ Å, the *C2/c* phase becomes vibrationally unstable and a monoclinic *Pc* phase exhibiting antiphase AFD O_6 rotations along the in-plane and out-of-plane directions and G-type AFM order is the ground state (labeled as R[001]+R[011]-G in Fig. 1b). While the space group of this latter phase is non-centrosymmetric, the estimated ferroelectric polarization is very small (~0.1 μC/cm^2, Fig. S5).

Interestingly, the monoclinic *Pc* phase, which is fully vibrationally stable in the relevant a_{in} interval (Fig. S6), appears to act as a *structural bridge* between the non-polar R[001]-G (*C2/c*) state stabilized under compressive strain and the ferroelectric Γ[110] +R[110]-G (*Ima2*) phase stabilized by small tensile strains. Moreover, complementary energy calculations indicate that the ground state of bulk SMO could either be *C2/c* or *Pc* (i.e., the zero-

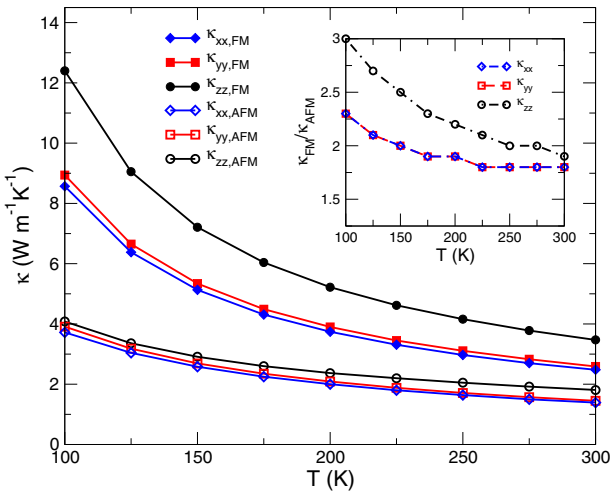

Fig. 2 Thermal conductivity expressed as a function of temperature for epitaxially strained SMO at $a_{in} = 3.92$ Å in the multiferroic *Ima2*-G and *Ima2*-FM phases. Inset: relative heat conductivity increase, κ_{FM}/κ_{AFM}, across the magnetoelectric phase transition in each tensor component.

temperature energy difference between these two polymorphs falls below our accuracy threshold of ≈ 1 meV/f.u.) instead of the assumed cubic $Pm\bar{3}m$ structure, since the energy minima of the two monoclinic phases are below that of the cubic phase by ≈ 5 meV per formula unit (Figure S3). Thus, according to our calculations, the non-polar ground state of bulk SMO should exhibit sizeable oxygen octahedral rotations accompanied by small (i.e., ~0.1°) monoclinic distortions along the [110] direction.

Giant multiphononic effects

From a phonons manipulation point of view, the most interesting region in the phase diagram of SMO thin films (Fig. 1a, b) is that around an in-plane lattice parameter of 3.92 Å, where the magnetoelectric *Ima2*-G → *Ima2*-FM phase transition occurs. This phase transition involves a change in magnetic order and a substantial increase in the electric polarization, which suggests that the magnetic and polar degrees of freedom are strongly coupled (i.e., large magnetoelectric interactions) and can be influenced by both external magnetic and electric fields. Potentially large electrophononic and magnetophononic effects (i.e., substantial lattice phonon variations driven by electric and magnetic fields), therefore, may simultaneously exist in that region of the phase diagram. On the other hand, the phase transitions triggered by compressive strain, despite their fundamental interest, seem to offer little multifunctional potential due to homogeneity in the magnetic features and lack of ferroelectricity.

In order to quantify the likely appearance of multiphononic effects (i.e., substantial lattice phonon variations driven by either electric or magnetic fields or combinations of both) around the magnetoelectric *Ima2*-G → *Ima2*-FM phase transition, we have computed with first-principles methods the thermal conductivity, κ, of the two involved phases at the critical in-plane lattice parameter of 3.92 Å. SMO is an insulating compound, and we obtain an electronic bandgap of approximately 2 eV for all the phases considered here (see the Supplementary Information for details). Hence, thermal transport can be assumed to be essentially carried out by phonons and we restrict ourselves to the lattice thermal conductivity. Our κ results obtained for the temperature interval $100 \le T \le 300$ K are shown in Fig. 2. Large and consistent variations in each component of the thermal conductivity are evidenced across the magnetoelectric transition at all the analyzed temperatures. At $T = 300$ K, for instance, practically a

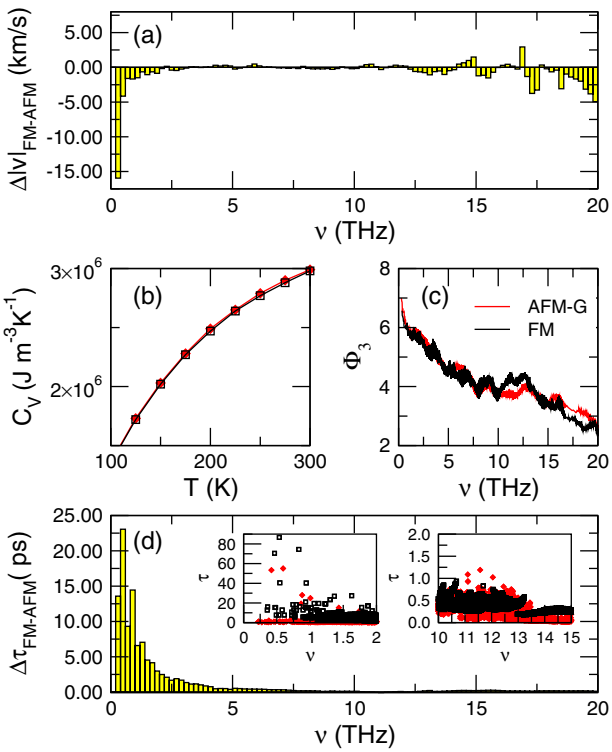

Fig. 3 Phononic analysis of epitaxially strained SMO at $a_{in} = 3.92$ Å in the multiferroic Ima2-G and Ima2-FM phases. **a** Difference between the phonon velocities of the *Ima2*-FM and *Ima2*-G phases averaged over frequency intervals of 0.2 THz. **b** Volumetric heat capacity expressed as a function of temperature for the AFM-G (filled red diamond) and FM (empty black squares) phases. **c** Phase-space and (**d**) mean phonon lifetime differences expressed as a function of phonon frequency; the insets show zoomed viewed on two different frequency windows. Panels (**a**, **b**) accounts for harmonic properties, while the results in panels (**c**, **d**) stem from anharmonic properties.

two-fold variation in κ is ascertained, *Ima2*-FM being the more conductive phase in all the cases (inset in Fig. 2). As the temperature is lowered, the heat conductivity differences between the two phases further increase, reaching for example a remarkable three-fold variation in one of the κ tensor components at $T = 100$ K. Next, we reveal the physical origins of such giant multiphononic effects.

Anharmonic spin-phonon couplings

In an effort to elucidate the atomistic mechanisms underlying the disclosed giant multiphononic effects, we have analyzed the variation of each quantity contributing to the thermal conductivity (Eq. (M1)) across the magnetoelectric phase transition. The results, shown in Fig. 3a–b, indicate that the predicted κ changes cannot be understood in terms of harmonic features (i.e., phonon velocities and heat capacity). In particular, phonon velocities are lower in the FM phase throughout the whole phonon spectrum and specially at low frequencies, which usually are the most relevant for heat transport. Meanwhile, the AFM and FM phases have a very similar heat capacity. The generalized softening of the phonon frequencies when moving from the AFM to the FM phase is indeed consistent with a phase transition volume expansion of ≈ 0.4% at $a_{in} = 3.92$ Å. Taken these effects alone, however, the thermal conductivity of the FM phase should be the lowest, which is at odds with our κ results shown in Fig. 2.

Let us now focus on the anharmonic processes. We start by analyzing the phase space, Φ_3, which accounts for all possible

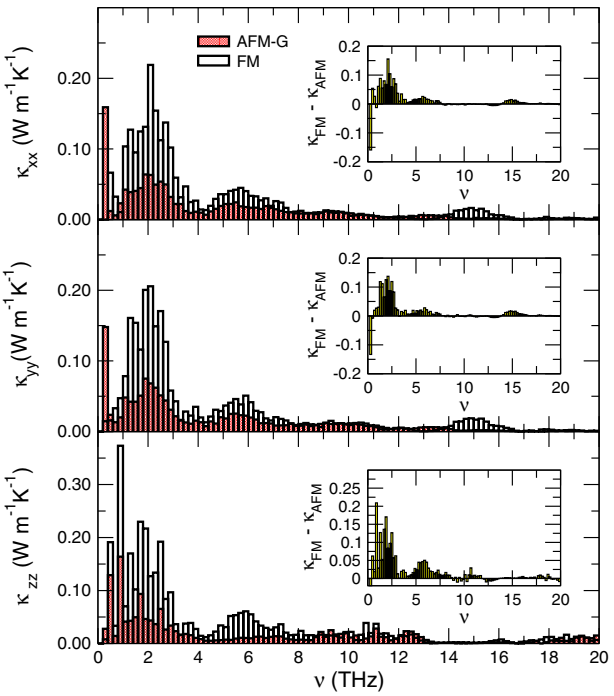

Fig. 4 Frequency-resolved thermal conductivity of strained SMO at $T = 300$ K in the FM and the AFM phases, averaged over frequency intervals of 0.2 THz. Insets: thermal conductivity differences, $\kappa_{FM} - \kappa_{AFM}$.

energy conserving three-phonon processes[28,29]. Φ_3 typically is inversely proportional to the lattice thermal conductivity because the more phonon-phonon collision processes are allowed, the higher the probability that a resistive scattering event takes place. Just like in the heat capacity case, the differences between the AFM and FM phases turn out to be not significant (Fig. 3c). In fact, the two Mn atoms in the *Ima2* unit cell are inequivalent both in the AFM and FM phases, thus the change in magnetic ordering does not noticeably alter the lattice symmetry, and thus the phase space of multi-phonon processes. It is worth noting that large magnetophononic effects have been recently predicted for FeRh across its metamagnetic AFM ↔ FM phase transition, and those have been ascribed to phase-space changes driven by crystal symmetry shifts[15]; similarly, phase-space broadening has been also proposed to be the fundamental cause of the significant κ reduction estimated for the ferroelectric perovskite $PbTiO_3$ upon reorientation of the polarization[10]. In the present case of multiphononic effects, however, phase-space variations induced by symmetry breaking do not constitute the main mechanism at play. (To prove this assertion, in the Supplementary Information we show a comparison between the phase-space of the FM and AFM phases of FeRh, where the AFM/FM differences drive the overall variation of the lattice thermal conductivity[15], and that of the FM and AFM phases of SMO).

Figure 3d shows the mean phonon lifetimes, τ, calculated for the AFM and FM phases of SMO and averaged over frequency slots of 0.2 THz. As it can be appreciated therein, the phonon lifetimes in the FM phase are systematically larger than those in the AFM phase. The τ differences are particularly significant in the low frequency region $\nu \lesssim 3$ THz. The shorter phonon lifetimes in the AFM phase indicate that this is more anharmonic than the FM phase. At variance with conventional spin-phonon couplings, in which spin ordering directly influences harmonic properties like phonon frequencies and phonon velocities, here we observe an original *anharmonic spin-phonon coupling* in which the magnetic degrees of freedom, coupled with the polar ones, govern the degree of anharmonicity in the material by drastically influencing its phonon lifetimes. The generally weaker anharmonic couplings in the FM phase can be partially originated by its slightly larger volume (≈1%) since structural expansions result in reduced phonon-phonon interactions at all orders. Nevertheless, the main driving factor behind such a large anharmonicity change appears to be the abovementioned structural rearrangements associated with the AFM ↔ FM phase transition, namely, the huge electric polarization and AFD O_6 tilts variations.

The frequency-resolved thermal conductivity displayed in Fig. 4 ($T = 300$ K) shows the contribution of each phonon mode to the three κ components, thus providing additional insight into the phonon transport properties of SMO thin films across the magneto-electric phase transition. In both AFM and FM *Ima2* phases, most of the heat is transported by low-energy phonons with frequencies in the range $\nu \lesssim 3$ THz; a small pocket of optical phonons with frequencies around 5 THz is also relevant in this regard. Throughout the whole frequency spectrum and for all components it is observed that $\kappa_{FM} > \kappa_{AFM}$, made the exception of the marginal frequency range $\nu < 0.4$ THz in which the AFM phase is more conductive (due to its very large phonon velocities, which overcompensate the shorter phonon lifetimes, Fig. 3). As it could be expected, for both magnetic phases we have $\kappa_{xx} \approx \kappa_{yy}$, because the two corresponding in-plane directions are practically equivalent from a crystallographic point of view. As for the out-of-plane direction, the largest κ increase with respect to the in-plane components (inset in Fig. 2) derives from low-frequency phonons, $\nu \lesssim 3$ THz, and from the narrow band of optical phonons centered around 5 THz already mentioned.

Functional aspects of multiphononic effects

As it was mentioned above, the *Ima2* AFM ↔ FM phase transition unraveled here for SMO thin films entails large changes in both the ferroelectric and magnetic degrees of freedom. These order-parameter variations suggest the possibility of dynamically tuning the thermal transport in SMO thin films by means of external electric and/or magnetic fields[30,31]. Next, we approximately quantify how large those external fields should be in practice, thus assessing the potential functionality of the reported giant multiphononic effects.

We approximately estimated the magnitude of the electric and magnetic fields required to induce the magnetoelectric phase transition of interest at zero temperature as follows:

$$E = \Delta U / \Delta(PV) \quad (1)$$

$$B = \Delta U / \Delta M\,, \quad (2)$$

where ΔU is the internal energy difference between the FM and the AFM phases, P the electric polarization, V the volume, and M the net magnetization (e.g., null in the AFM phase). Note that this estimate provides us with a lower limit for the coercive fields, since in practice there will be energy barriers to overcome that we are disregarding here (see discussion below). However, these values give an idea of the order of magnitude of the fields required to trigger the phase transitions. Figure 5a shows our coercive field results expressed as a function of the in-plane lattice parameter. The interest of conveniently adjusting a_{in} is clear, that is, to induce the appearance of electrophononic and magneto-phononic effects via the application of small external fields. For instance, at $a_{in} = 3.92$ Å we obtain $E = 32$ kV/cm and $B = 1.4$ T, which are values that can be ordinarily reached in practice and hence hold promise from an applied point of view. (We note that the in-plane lattice parameter at which ΔE exactly amounts to zero is slightly above 3.92 Å, see the inset in Fig. 5a). Indeed, in the simplified model here considered, as $\Delta E \to 0$ the fields required to induce the phase transition become vanishingly small. Conversely, as we move away from $a_{in} = 3.92$ Å the size of the triggering fields rapidly increase (e.g., 1367 kV/cm[1] and 72 T at $a_{in} = 3.90$ Å).

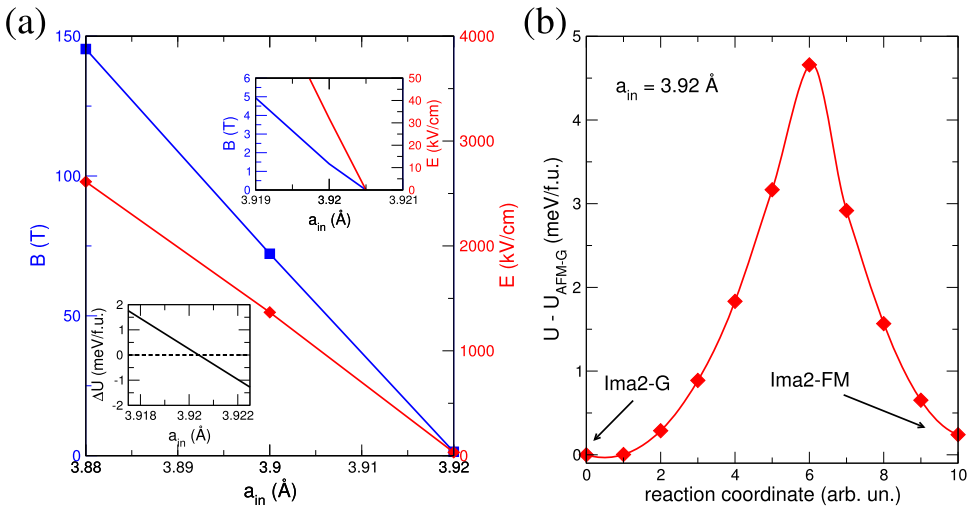

Fig. 5 Multifunctional analysis of epitaxially strained SMO. a Approximate estimation of the electric and magnetic fields needed to induce the magnetoelectric *Ima2*-G ↔ *Ima2*-FM phase transition in SMO thin films expressed as a function of the in-plane lattice parameter. Inset (bottom): Energy difference between the FM and AFM phases expressed as a function of a_{in}. Inset (top): Magnification of the phase-transition driving electric and magnetic fields near 3.92 Å. **b** Approximate estimation of the energy barrier involved in field-driven switching between the *Ima2*-G ↔ *Ima2*-FM phases.

A similar situation to the one just described has been recently reported for the ferroelectric perovskite $PbTiO_3$, in which an appropriately selected biaxial strain leads to the effortless rotation of the polarization and consequent realization of large electrophononic effects[13]. In the case of SMO thin films, epitaxial strain enables the concerted appearance of substantial electrophononic and magnetophononic responses that join together to render giant multiphononic effects.

A rough estimate of the switching barrier can be made by interpolating several intermediate configurations between the isostructural AFM and FM phases and calculating the energy of each of them in their most favorable magnetic state. We have carried out such calculations right at $a_{in} = 3.92$ Å, which provide an overestimation of the real transition energy barrier since we have not optimized the transition path, finding that the barrier amounts to around 5 meV per formula unit (Fig. 5b) or equivalently, 20 meV per unit cell. These results suggest that in practice it should be feasible to realize the proposed field-induced phase transformation in the single-domain setup considered here (magnetic/polar domain-related switching effects are not accounted for, though the presence of multidomains would further decrease the size of the involved coercive fields[32]). It is also noted that the estimated transition energy barrier between the AFM and FM phases, namely, ≈ 20 meV per unit cell, is consistent with the experimental fact that SMO becomes paramagnetic at temperatures slightly below room temperature[18–20], since the thermal fluctuations at $T = 300$ K amount to 26 meV. These fluctuations can be supressed by adopting slightly smaller a_{in} values, which would result in slightly larger magnetic driving fields and thus switching energy barriers.

In conclusion, by means of first-principles calculations we predict the existence of giant multiphononic effects in the non-polar perovskite oxide SMO when it is subjected to suitable epitaxial strain conditions. Upon moderate tensile strains, SMO becomes multiferroic and can be brought to the verge of a magnetoelectric phase transition in which the magnetic spin ordering and electric polarization change abruptly. The relative thermal conductivity changes associated with such a multiferroic transformation can be as large as 200% and, most remarkably, can be externally induced by small electric and magnetic fields of the order of 10 kV/cm and 1 T, respectively. We explain the physical origins of these multiphononic effects and thermal transport functionality in terms of anharmonic spin-phonon couplings that act directly on the mean lifetime of phonons. In addition, we revisited the phase diagram of SMO thin films with the finding that several monoclinic and previously overlooked non-polar phases can be stabilized under compressive strains and probably also in bulk (although they offer little interest in terms of dynamical control of the heat conductivity due to their null net magnetizations and polarizations). Similar multiphononic effects to those reported here for SMO can be expected to occur also in other multiferroic perovskite thin films in which the combined action of epitaxial strain and moderate external fields may induce magnetoelectric phase transitions (e.g., $BiFeO_3$ and $BiCoO_3$)[24]. Therefore, we anticipate that the present computational study will stimulate experimental realizations of dynamical manipulation of phonons in functional perovskite oxides with potential for applications in the innovative field of phononic information technologies and devices.

METHODS

First-principles calculations

We performed density functional theory (DFT) calculations with the VASP code[33] and projector augmented waves[34,35] with an energy cutoff of 650 eV and the generalized-gradient approximation PBEsol[36]. The following electrons were explicitly treated as valence: Sr $4s^2 4p^6 5s^2$, Mn $3p^6 3d^5 4s^2$, and O $2s^2 2p^4$. The Hubbard-U scheme derived by Dudarev et al.[37] was used to deal with the 3*d* electrons in the Mn atoms and, as done in previous works, a *U* value of 3 eV was adopted[37]. We have performed several tests to assess the influence of the adopted DFT exchange-correlation functional and *U* value on our theoretical predictions (see the Supplementary Information); the structural properties and energy ranking of the competing phases, however, remain invariant in most a_{in} cases.

We employed a 20–atom unit cell for our energy and structure calculations corresponding to a $\sqrt{2} \times \sqrt{2} \times 2$ perovskite oxide supercell, in which the long axis, *c*, was oriented out-of-plane (i.e., epitaxial strain was applied on the *ab* plane). A **k**-point grid of $10 \times 10 \times 7$ was used for sampling of the first Brillouin zone. As it is usually done, epitaxial strain was reproduced by fixing the length and angle of the two in-plane lattice vectors to a fixed value, namely, $a = b = a_{in}$ and $\widehat{ab} = 90^\circ$, and fully optimizing the out-of-

plane lattice vector **c**[38]. All the atomic positions were optimized until the maximum atomic force component was lower than 0.005 eV/Å. Electric polarizations were calculated with the Born effective charges method[39].

We computed the second- and third-order interatomic force constants by finite differences[29,40] in a $2 \times 2 \times 2$ supercell, amounting to 160 atoms, with a cutoff of 3.3 Å in the three-phonon scattering processes, which spans up to the eighth nearest neighbors in the bulk orthorhombic *Ima2* phase. We then solved the phonon Boltzmann Transport Equation (BTE) to obtain the thermal conductivity, including scattering from isotopic disorder through the model of Tamura[41]. Preliminary tests showed that converged results are achieved using the Relaxation Time Approximation (RTA) and a **q**-point grid of $12 \times 12 \times 12$ (see the Supplementary Information). The lattice thermal conductivity was then estimated as:

$$\kappa_{ij} = \sum_{\lambda} \kappa_{ij,\lambda} = C \sum_{\lambda} f_{\lambda}(f_{\lambda}+1)(h\nu_{\lambda})^2 \tau_{\lambda} v_{i,\lambda} v_{j,\lambda} = \frac{1}{N} \sum_{\lambda} C_{\lambda} \tau_{\lambda} v_{i,\lambda} v_{j,\lambda} \quad \text{(M1)}$$

where i and j run over the Cartesian directions x, y, and z. $C^{-1} = k_B T^2 \Omega N$, where k_B, h, T, Ω and N represent, respectively, the Boltzmann's constant, Planck's constant, temperature, volume of the unit cell, and number of **q**-points. The sum runs over all phonon modes, the index λ including both **q**-point and phonon band. f_{λ} is the equilibrium Bose-Einstein distribution function, and v_{λ} and $v_{i,\lambda}$ are, respectively, the frequency and group velocity of phonon λ. C_{λ} is the volumetric heat capacity of the phonon mode λ, which contributes to the volumetric heat capacity of the crystal like $C_P = 1/N \Sigma_{\lambda} C_{\lambda}$.

Within this formalism, the phonon lifetimes discussed in the text are computed as the inverse of the three-phonon scattering rates:

$$\Gamma^{+}_{\lambda\lambda'\lambda''} = \frac{\hbar\pi}{4} \frac{f_{\lambda'} - f_{\lambda''}}{\omega_{\lambda}\omega_{\lambda'}\omega_{\lambda''}} |V^{+}_{\lambda\lambda'\lambda''}|^2 \delta(\omega_{\lambda} + \omega_{\lambda'} - \omega_{\lambda''}) \quad \text{(M2)}$$

$$\Gamma^{-}_{\lambda\lambda'\lambda''} = \frac{\hbar\pi}{4} \frac{f_{\lambda'} - f_{\lambda''} + 1}{\omega_{\lambda}\omega_{\lambda'}\omega_{\lambda''}} |V^{-}_{\lambda\lambda'\lambda''}|^2 \delta(\omega_{\lambda} - \omega_{\lambda'} - \omega_{\lambda''}) \quad \text{(M3)}$$

where $\Gamma^{+}_{\lambda\lambda'\lambda''}$ and $\Gamma^{-}_{\lambda\lambda'\lambda''}$ correspond to absorption and emission processes, respectively. $V^{+}_{\lambda\lambda'\lambda''}$ and $V^{-}_{\lambda\lambda'\lambda''}$ are the scattering matrix elements that are computed from the anharmonic third-order IFCs[29].

DATA AVAILABILITY

The data that support the findings of this study are available from the authors upon reasonable request.

Received: 3 January 2023; Accepted: 25 May 2023;
Published online: 03 June 2023

REFERENCES

1. Moore, A. L. & Shi, L. Emerging challenges and materials for thermal management of electronics. *Mater. Today* **17**, 163 (2014).
2. Zebarjadi, M., Esfarjani, K., Dresselhaus, M. S., Ren, Z. F. & Chen, G. Perspectives on thermoelectrics: from fundamentals to device applications. *Energy Environ. Sci.* **5**, 5147 (2012).
3. Benenti, G., Casati, G., Saito, K. & Whitney, R. S. Fundamental aspects of steady-state conversion of heat to work at the nanoscale. *Phys. Rep.* **694**, 1 (2017).
4. Terraneo, M., Peyrard, M. & Casati, G. Controlling the energy flow in nonlinear lattices: a model for a thermal rectifier. *Phys. Rev. Lett.* **88**, 094302 (2002).
5. Li, B., Wang, L. & Casati, G. Negative differential thermal resistance and thermal transistor. *Appl. Phys. Lett.* **88**, 143501 (2006).
6. Li, N. et al. Colloquium: phononics: manipulating heat flow with electronic analogs and beyond. *Rev. Mod. Phys.* **84**, 1045 (2012).
7. Volz, S. et al. Nanophononics: state of the art and perspectives. *Eur. Phys. J. B* **89**, 15 (2016).
8. Huber, W. H., Hernandez, L. M. & Goldman, A. M. Electric field dependence of the thermal conductivity of quantum paraelectrics. *Phys. Rev. B* **62**, 8588 (2000).
9. Qin, G., Qin, Z., Yue, S.-Y., Yan, Q.-B. & Hu, M. External electric field driving the ultra-low thermal conductivity of silicene. *Nanoscale* **9**, 7227 (2017).
10. Seijas-Bellido, J. A., Aramberri, H., Íñiguez, J. & Rurali, R. Electric control of the heat flux through electrophononic effects. *Phys. Rev. B* **97**, 184306 (2018).
11. Torres, P., Seijas-Bellido, J. A., Escorihuela-Sayalero, C., Íñiguez, J. & Rurali, R. Theoretical investigation of lattice thermal conductivity and electrophononic effects in $srtio_3$. *Phys. Rev. Mater.* **3**, 044404 (2019).
12. Seijas-Bellido, J. A., Íñiguez, iJ. & Rurali, R. Anisotropy-driven thermal conductivity switching and thermal hysteresis in a ferroelectric. *Appl. Phys. Lett.* **115**, 192903 (2019).
13. Torres, P., Íñiguez, J. & Rurali, R. Giant electrophononic response in $pbtio_3$ by strain engineering. *Phys. Rev. Lett.* **123**, 185901 (2019).
14. Yang, Z., Yuan, K., Meng, J. & Hu, M. Electric field tuned anisotropic to isotropic thermal transport transition in monolayer borophene without altering its atomic structure. *Nanoscale* **12**, 19178 (2020).
15. Cazorla, C. & Rurali, R. Dynamical tuning of the thermal conductivity via magnetophononic effects. *Phys. Rev. B* **105**, 104401 (2022).
16. Fiebig, M., Lottermoser, T., Meier, D. & Trassin, M. The evolution of multiferroics. *Nat. Rev. Mater.* **1**, 16046 (2022).
17. Hou, H., Qian, S. & Takeuchi, I. Materials, physics and systems for multicaloric cooling. *Nat. Rev. Mater.* **7**, 633 (2022).
18. Takeda, T. & Ōhara, S. Magnetic structure of the cubic perovskite type $SrMnO_3$. *J. Phys. Soc. Jpn.* **37**, 275 (1974).
19. Chmaissem, O. et al. Relationship between structural parameters and the Néel temperature in $Sr_{1-x}Ca_xMnO_3$ ($0 \lesssim x \lesssim 1$) and $Sr_{1-y}Ba_yMnO_3$ ($y \lesssim 0.2$). *Phys. Rev. B* **64**, 134412 (2001).
20. Maurel, L. et al. Nature of antiferromagnetic order in epitaxially strained multiferroic $srmno_3$ thin films. *Phys. Rev. B* **92**, 024419 (2015).
21. Lee, J. H. & Rabe, K. M. Epitaxial-strain-induced multiferroicity in $SrMnO_3$ from first principles. *Phys. Rev. Lett.* **104**, 207204 (2010).
22. Escorihuela-Sayalero, C., Diéguez, O. & Íñiguez, J. Strain engineering magnetic frustration in perovskite oxide thin films. *Phys. Rev. Lett.* **109**, 247202 (2012).
23. Cazorla, C. & Íñiguez, J. Giant direct and inverse electrocaloric effects in multiferroic thin films. *Phys. Rev. B* **98**, 174105 (2018).
24. Menéndez, C., Chu, D. & Cazorla, C. Oxygen-vacancy induced magnetic phase transitions in multiferroic thin films. *npj Comput Mater* **6**, 76 (2020).
25. Kamba, S. et al. Strong spin-phonon coupling in infrared and raman spectra of $SrMnO_3$. *Phys. Rev. B* **89**, 064308 (2014).
26. Guo, J. W. et al. Strain-induced ferroelectricity and spin-lattice coupling in $SrMnO_3$ thin films. *Phys. Rev. B* **97**, 235135 (2018).
27. Sando, D. et al. Epitaxial ferroelectric oxide thin films for optical applications. *Appl. Phys. Rev.* **5**, 041108 (2018).
28. Lindsay, L. & Broido, D. A. Three-phonon phase space and lattice thermal conductivity in semiconductors. *J. Phys.: Condens. Matter* **20**, 165209 (2008).
29. Li, W., Carrete, J., Katcho, N. A. & Mingo, N. ShengBTE: a solver of the Boltzmann transport equation for phonons. *Comp. Phys. Commun.* **185**, 1747 (2014).
30. Nikitin, S. et al. The magnetocaloric effect in $Fe_{49}Rh_{51}$ compound. *Phys. Lett. A* **148**, 363 (1990).
31. Stern-Taulats, E. et al. Barocaloric and magnetocaloric effects in $Fe_{49}Rh_{51}$. *Phys. Rev. B* **89**, 214105 (2014).
32. Tagantsev, A. K., Cross, L. E. & Fousek, J. *Domains in Ferroic Crystals and Thin Films* (Springer New York, NY, 2010)
33. Kresse, G. & Furthmüller, J. Efficient iterative schemes for ab initio total-energy calculations using a plane-wave basis set. *Phys. Rev. B* **54**, 11169 (1996).
34. Blöchl, P. E. Projector augmented-wave method. *Phys. Rev. B* **50**, 17953 (1994).
35. Kresse, G. & Joubert, D. From ultrasoft pseudopotentials to the projector augmented-wave method. *Phys. Rev. B* **59**, 1758 (1999).
36. Perdew, J. P. et al. Restoring the density-gradient expansion for exchange in solids and surfaces. *Phys. Rev. Lett.* **100**, 136406 (2008).
37. Dudarev, S. L., Botton, G. A., Savrasov, S. Y., Humphreys, C. J. & Sutton, A. P. Electron-energy-loss spectra and the structural stability of nickel oxide: An LSDA +U study. *Phys. Rev. B* **57**, 1505 (1998).
38. Cazorla, C. & Stengel, M. Electrostatic engineering of strained ferroelectric perovskites from first principles. *Phys. Rev. B* **92**, 214108 (2015).
39. Menéndez, C. & Cazorla, C. Giant thermal enhancement of the electric polarization in ferrimagnetic $BiFe_{1-x}Co_xO_3$ solid solutions near room temperature. *Phys. Rev. Lett.* **125**, 117601 (2020).
40. Togo, A. & Tanaka, I. First principles phonon calculations in materials science. *Scr. Mater.* **108**, 1 (2015).
41. Tamura, S. Isotope scattering of dispersive phonons in ge. *Phys. Rev. B* **27**, 858 (1983).

ACKNOWLEDGEMENTS

We acknowledge financial support by MCIN/AEI/10.13039/501100011033 under grant PID2020-119777GB-I00, the Ramón y Cajal fellowship RYC2018-024947-I and the Severo Ochoa Centres of Excellence Program (CEX2019-000917-S), and by the Generalitat de Catalunya under grant no. and 2017 SGR 1506. Calculations were performed at the Centro de Supercomputación de Galicia (CESGA) within action FI-2022-1-0012 of the Red Española de Supercomputación (RES). We also thank the support of the Luxembourg National Research Fund through project FNR/C18/MS/12705883/REFOX (J.Í.).

AUTHOR CONTRIBUTIONS

C.C. and R.R. conceived the project. C.C. and R.R carried the DFT and the heat transport calculations, respectively. J.Í. and M.S. provided critical input about the phase diagram and supervised those calculations. All authors contributed to discussions and the final manuscript.

COMPETING INTERESTS

The authors declare no competing interests.

ADDITIONAL INFORMATION

Supplementary information The online version contains supplementary material available at https://doi.org/10.1038/s41524-023-01057-w.

Correspondence and requests for materials should be addressed to Riccardo Rurali.